KeAi

CHINESE ROOTS
GLOBAL IMPACT

#### Contents lists available at ScienceDirect

# Petroleum Science

journal homepage: www.keaipublishing.com/en/journals/petroleum-science



# Original Paper

# Integrating well logs, 3D seismic, and earthquake data for comprehensive prediction of 3D in-situ stress orientations: A case study from the Weiyuan area in the Sichuan Basin, China



Huan Cao <sup>a</sup>, Yang Zhao <sup>a, \*</sup>, Hai-Chao Chen <sup>a</sup>, Le-Le Zhang <sup>a</sup>, Cheng-Gang Xian <sup>a</sup>, Ji-Dong Yang <sup>b</sup>, Lu Liu <sup>c</sup>

- <sup>a</sup> State Key Laboratory of Petroleum Resources and Engineering, and Unconventional Petroleum Research Institute, China University of Petroleum (Beijing), Beijing, 102249, China
- <sup>b</sup> Department of Geophysics, China University of Petroleum (East China), Qingdao, 266580, Shandong, China
- <sup>c</sup> Aramco Beijing Research Center, Aramco Asia, Beijing, 100102, China

#### ARTICLE INFO

# Article history: Received 25 April 2024 Received in revised form 19 June 2024 Accepted 15 July 2024 Available online 17 July 2024

Edited by Meng-Jiao Zhou

Keywords: In-situ stress orientation SHmax Azimuthal velocity anisotropy Focal source mechanism Formation micro-imager

#### ABSTRACT

Determining the orientation of in-situ stresses is crucial for various geoscience and engineering applications. Conventional methods for estimating these stress orientations often depend on focal mechanism solutions (FMSs) derived from earthquake data and formation micro-imager (FMI) data from well logs. However, these techniques can be costly, depth-inaccurate, and may lack spatial coverage. To address this issue, we introduce the use of three-dimensional (3D) seismic data (active sources) as a lateral constraint to approximate the 3D stress orientation field. Recognizing that both stress and fracture patterns are closely related to seismic velocity anisotropy, we derive the orientation of azimuthal anisotropy from multi-azimuth 3D seismic data to compensate for the lack of spatial stress orientation information. We apply our proposed workflow to a case study in the Weiyuan area of the Sichuan Basin, China, a region targeted for shale gas production. By integrating diverse datasets, including 3D seismic, earthquakes, and well logs, we develop a comprehensive 3D model of in-situ stress (orientations and magnitudes). Our results demonstrate that the estimated anisotropy orientations from 3D seismic data are consistent with the direction of maximum horizontal principal stress (SHmax) obtained from FMIs. We analyzed 12 earthquakes (magnitude > 3) recorded between 2016 and 2020 for their FMSs and compressional axis (Paxis) orientations. The derived SHmax direction from our 3D stress model is 110° ES (East-South), which shows excellent agreement with the FMSs (within 3.96°). This close alignment validates the reliability and precision of our integrated method for predicting 3D SHmax orientations.

© 2024 The Authors. Publishing services by Elsevier B.V. on behalf of KeAi Communications Co. Ltd. This is an open access article under the CC BY-NC-ND license (http://creativecommons.org/licenses/by-nc-nd/4.0/).

#### 1. Introduction

It's well-known that the orientation of in-situ stress plays a critical role in unconventional developments such as pattern layouts, optimizing well trajectories, designing hydraulic fracturing operations, and mitigating wellbore instability (Cornet and Valette, 1984; Tingay et al., 2009; Zoback, 2007; Feng et al., 2018). The orientations of in-situ stress are often described as the direction of the SHmax (Delorey et al., 2021; Lundstern and Zoback, 2016, 2020). We will systematically measure the in-situ stress direction

\* Corresponding author. E-mail address: zhaoyang@cup.edu.cn (Y. Zhao). across three different scales, following a calibrated sequence.

Firstly, at the core scale ( $10^{-3}$ – $10^{-2}$  m), the common practices in this regard often involve mechanical tests such as paleomagnetic core orientation, differential strain, acoustic emission Kaiser effect, and acoustic anisotropy (Haimson and Song, 1995; Haimson and Fairhurst, 1967; Kaiser, 1957). Teufel (1983) invented a device based on the Anelastic strain recovery (ASR), which can determine the direction of in-situ stress in deep geological formations. Zhang et al. (2022, 2023) utilized ASR for core stress measurement and estimated the full stress tensor of the core. The stress direction of the area is matched well with the FMSs. Subsequently, scholars have employed the differential strain curve analysis (DSCA) in laboratory settings, applying confining pressure to rock samples

from various azimuths to ascertain the stress direction. The principle of the differential wave velocity analysis (DWVA) is analogous to that of the DSCA. Scholars analyze acoustic wave velocities under varying stress states and orientations to accurately estimate the direction of stress (Haimson and Song, 1995; Haimson and Fairhurst, 1967). Laubach et al. (1992) employed axial point load tests to analyze stress direction and observed a bimodal distribution pattern in anisotropic strength. Han et al. (2020) proposed an innovative approach that combines paleomagnetic core orientation tests with acoustic anisotropy assessments. Then, we calibrated the one-dimensional (1D) well logs using the data obtained from the core samples and ensuring an accurate representation of subsurface conditions along the wellbore. This calibration enhances the reliability of well logs for subsequent analyses aimed at determining in-situ stress direction at this fine scale. It serves as a foundational step, paving the way for measurements at larger scales and ensuring a consistent and accurate multi-scale approach to stress measurement. However, laboratory testing is simple, their accuracy is limited. The main source of this error lies in the variability of rock samples.

Subsequently, due to the advantage of longitudinal resolution at the scale of 1D well logging  $(10^{-1}-10^1 \text{ m})$ , research on measuring stress directions utilizing image logs (Ezati and Soleimani, 2014; Jonaghani et al., 2019; Paul et al., 2018; Ziaie et al., 2023) have been heavily studied, including wellbore image analysis, hydraulic fracture monitoring, wellbore microseismic monitoring, and formation imaging logging (Bao et al., 2009; Li et al., 2012; Han et al., 2020; Hou et al., 2014). Leeman et al. (1964) utilized borehole breakouts (BOS) to determine stress orientation. Haimson and Fairhurst (1967) conducted testing and research on stress orientation using Micro-hydraulic fracturing (HF) technology, laying the foundation for its subsequent engineering applications. Hornby (1989) studied shear velocity anisotropy to infer the SHmax orientation. Jonaghani et al. (2019) used a dipole sonic imager (DSI) across wells to enhance comprehension of structural geology. Ziaie et al. (2023) used drilling data to estimate the horizontal in-situ stress magnitude and orientation. These borehole techniques are employed to discern rock formation properties, utilizing high-resolution imaging through the assessment of parameters like resistivity, natural gamma rays, and acoustic velocity within borehole walls. These data capture detailed structural features and fault orientations, significantly enhancing insights into geological formations. Realtime monitoring facilitates dynamic adjustments to drilling strategies. Notably, the drilling-induced fracture orientation aligns with the SHmax direction, providing valuable information about the stress regime and structural characteristics of the rock formations. On the other hand, these methods often suffer from their high cost and limited drilling depths (<10 km). A borehole only reflects the stress conditions at a single specific site which may underrepresent the stress fields with lateral variations (Cui et al., 2014; Zoback, 2007). We have used the calibrated 1D well logging curves to calibrate 3D seismic. Integrating wellbore-scale data with regional geological and geophysical information, this multiscale approach offers a comprehensive understanding of the in-situ stress direction, crucial for optimizing reservoir management.

Finally, at the region scale  $(10^2-10^5 \text{ m})$ , earthquake-based FMSs are widely used for predicting larger-scale in-situ stress orientations. This method involves constructing an internal earth velocity structure model as the basis for computing Green's functions. Iterative calculations, aiming to find the optimal Green's function, involve adjusting seismic source parameters (depth, magnitude, and mechanism) to closely match simulated Green's functions with observed seismic waveforms (Long et al., 2019). The process includes comparing multiple simulations and selecting the most

suitable seismic source mechanism parameters. Amemoutou et al. (2021) analyzed the regional orientations via earthquakes ( $M_{\rm W} \leq 4.9$ ) in southern Kansas. Zhang et al. (2022) calculated the FMSs of 124 earthquakes ( $M_{\rm S} \geq 3.0$ ) in the Changning area in the Sichuan Basin since 2007 and provided the orientations of stress fields. FMSs require substantial seismic activity monitored by a robust network to provide the correct earthquake depths as well as their source mechanisms (Heidbach et al., 2018).

These abovementioned across-scale measurements experience a scale gap  $(10^1-10^3 \text{ m})$ . To fill the measurement gap and bridge between FMIs and FMSs (Fig. 1), we integrate the 3D seismic into FMSs/FMIs to determine the stress orientation. The 3D seismic may effectively compensate for high costs (boreholes) and inaccurate depths (FMSs). Specifically, we assume the azimuthal anisotropy of seismic velocity aligns closely with the SHmax direction in the study area. 3D multi-azimuth seismic is used to compute the azimuthal anisotropy via the elliptical fitting method to build the original orientations of the 3D stress field. 26 earthquakes ( $M_L > 3$ ) from 2016 to 2020 are selected to calculate the FMSs and their P-axes. The resultant SHmax direction of the 3D stress model is then calibrated by the FMIs from two well-logs and 12 FMSs via co-krigging.

# 2. Geological setting of the Weiyuan area in the Sichuan Basin, China

The Sichuan Basin, as depicted in Fig. 2, is characterized by its extensive fault and fold structures, including prominent geological features such as the Longmenshan and Xianshuihe faults. The Weiyuan area, situated in the mid-southern part of the basin, is a key region for shale gas production. The stratigraphic reservoirs relevant for shale gas, ranging from the Upper Ordovician Wufeng Formation  $(O_3w)$  to the Lower Silurian Longmaxi Formation  $(S_1l)$ , are deeply buried, with depths spanning from 1.2 to 3.6 km (Liu and Wang, 2016; Zou et al., 2015). Since 2015, there has been a marked increase in shale gas production within the Weiyuan area. This uptick in production has likely had a significant impact on the local stress regimes, necessitating precise and comprehensive methods for predicting the orientations of in-situ stresses to ensure safe and efficient extraction operations (Chu and Sheng, 2023; Sheng et al., 2022).

In this section, we conduct a multifaceted analysis of the SHmax orientations within the Weiyuan area, drawing on three distinct datasets: well logs, 3D seismic, and earthquake records. Our initial approach involves the interpretation of FMI log data from two wells to discern the spatial distribution of SHmax orientations at those specific locations. Following this, we apply linear slip theory under the presumption that fracture directions coincide with the SHmax orientations. We use the azimuthal velocity anisotropy to perform an elliptical fit of the azimuthal P-wave phase velocity, which enables us to infer the 3D fracture orientations. The final step entails the cut and paste (CAP) waveform inversion technique on FMSs derived from earthquakes and their associated P-axes. Through an exhaustive assessment of SHmax orientations and an integration of stress across different scales, we can build a comprehensive in-situ stress model (orientations and magnitudes) in the study area. The detailed workflow is illustrated in Fig. 3 below.

#### 3. Multi-sources data and methodology

#### 3.1. Borehole measurements and FMIs

We first discuss the borehole information in terms of stress orientations. BOS are typically characterized as fractures that form

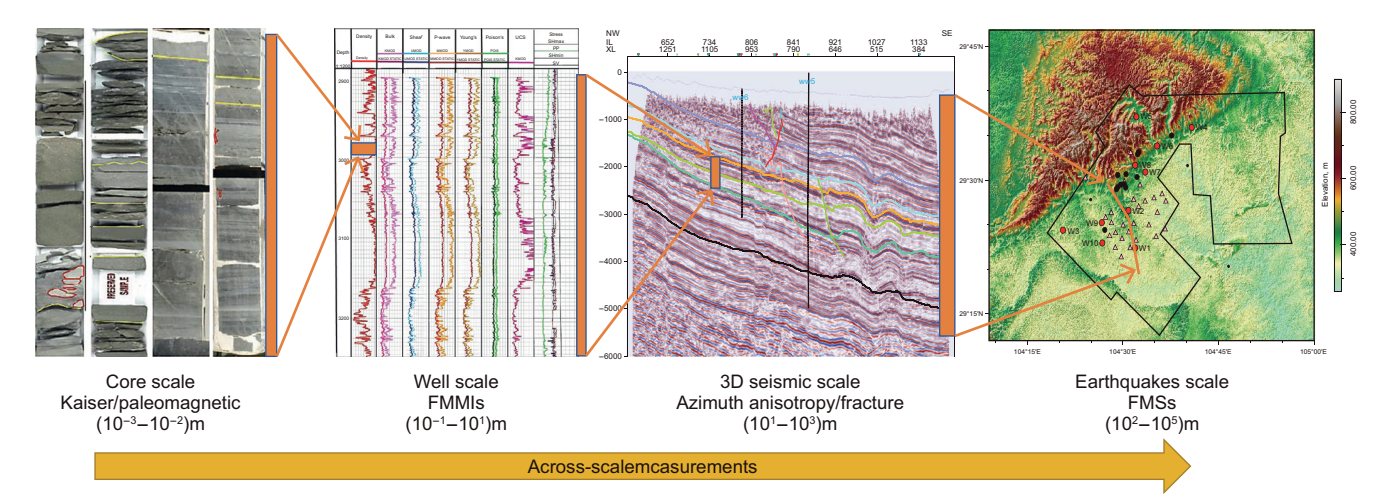
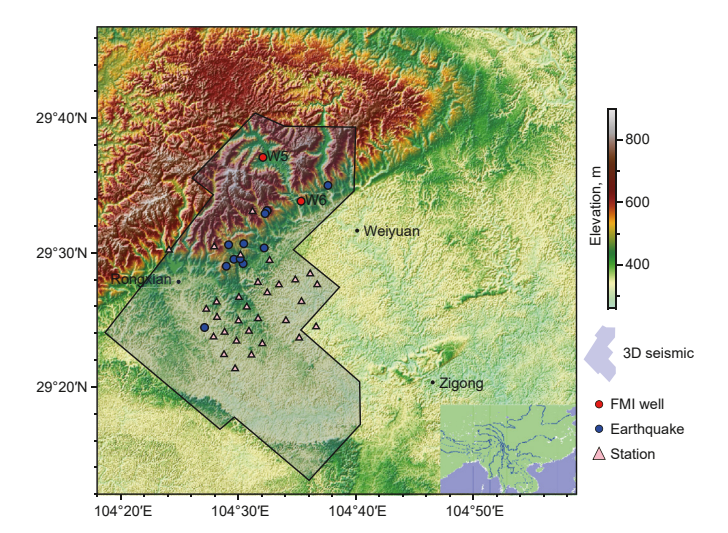


Fig. 1. The cross-scale measurement of stress field orientations illustrates how stress orientations are measured and analyzed across different scales.



**Fig. 2.** The regional data encompasses information on FMI logging, earthquakes, and 3D seismic. Two FMI imaging logging wells are depicted by red circles, while earthquakes are represented by blue circles. Additionally, the light blue shaded area delineates the spatial extent of 3D seismic, covering approximately 1000 km<sup>2</sup>, and mobile seismic stations are denoted by pink triangles in the Weiyuan area.

around the borehole and align with the direction of the minimum horizontal stress (SHmin). These breakouts occur when the compressive strength of the rock surrounding the wellbore is exceeded by the circumferential stress. On the other hand, when the circumferential stress exceeds the tensile strength of the wellbore wall, it leads to the formation of drilling-induced fractures (DIFs), which are oriented parallel to the maximum horizontal stress (SHmax). These fractures can be identified on image logs within the wellbore, displaying a circular to elliptical pattern, and in this study, an FMI image log was used for analysis. In the study area, two FMI logging were conducted within the work area, situated in the northern part with a shallow burial depth. Fig. 4 demonstrates the azimuth and dip of DIFs for Wells W5 and W6, indicating a relatively consistent SHmax orientation within the target layer of Well W5. However, at a depth of 2500 m, the fracture azimuth in Well W6 displayed a notably different orientation compared to Well W5, suggesting a complex structural stress evolution in the region.

#### 3.2. 3D seismic and azimuthal anisotropy

We next examine the 3D seismic data in the context of stress orientations. A comprehensive 3D seismic survey covering an area of 1000 square kilometers was conducted in the Weiyuan region in the year 2018. We perform VVAZ (velocity versus azimuth) and AVAZ (amplitude versus azimuth) analyses, including bandpass filtering, radon transform, deconvolution, gain equalization, and stack azimuth. Three seismic partial angle stacks with ranges of 5°, 15°, and 25° were generated from the full azimuth-dependent stack prestack time migration (PSTM) gathers. The center azimuth angles are 0°, 60°, 120°, 180°, 240°, and 300°, respectively, as shown in Fig. 5.

We conducted AVO inversion independently for each azimuth, as illustrated in Fig. 6. This approach allowed us to analyze the seismic response from different angles, providing a comprehensive understanding of the subsurface properties. Importantly, we observed a clear seismic alignment with the well, indicating a correlation between the seismic data and the well data. This alignment further validates the reliability of our AVO inversion results and enhances our confidence in the geological interpretations derived from the seismic data.

Subsequently utilize the resulting azimuthal P-wave phase velocities to ellipse fitting for estimating anisotropic parameters. There are numerous methods for predicting anisotropic parameters, with recent research frequently utilizing the azimuthal PPwave reflection coefficients to estimate crack parameters. For example, Pan et al. (2021) introduced a new azimuthal PP-wave reflection coefficient and an azimuthal EI equation, employing divisions in EI angle and azimuth to gauge fluid and frame indicators. Similarly, Chen and Innanen (2023) derived the PP-wave reflection coefficient and azimuthal elastic impact (AEI) as functions of frame weaknesses, assessing normal and tangential fracture weaknesses through azimuthal variations in partially stacked seismic data. However, these methods only predict the strength of fracture development, not the direction of fractures. To address this limitation, our study uses the azimuthal anisotropy of P-wave phase velocity to predict HTI parameters. Analytical formulations demonstrate that azimuthal P-wave velocity better aligns with HTI elliptical fitting compared to the azimuthal reflection coefficient. To tackle the ill-posed issues in the simultaneous inversion of elastic and anisotropic parameters, we adopt a two-step inversion

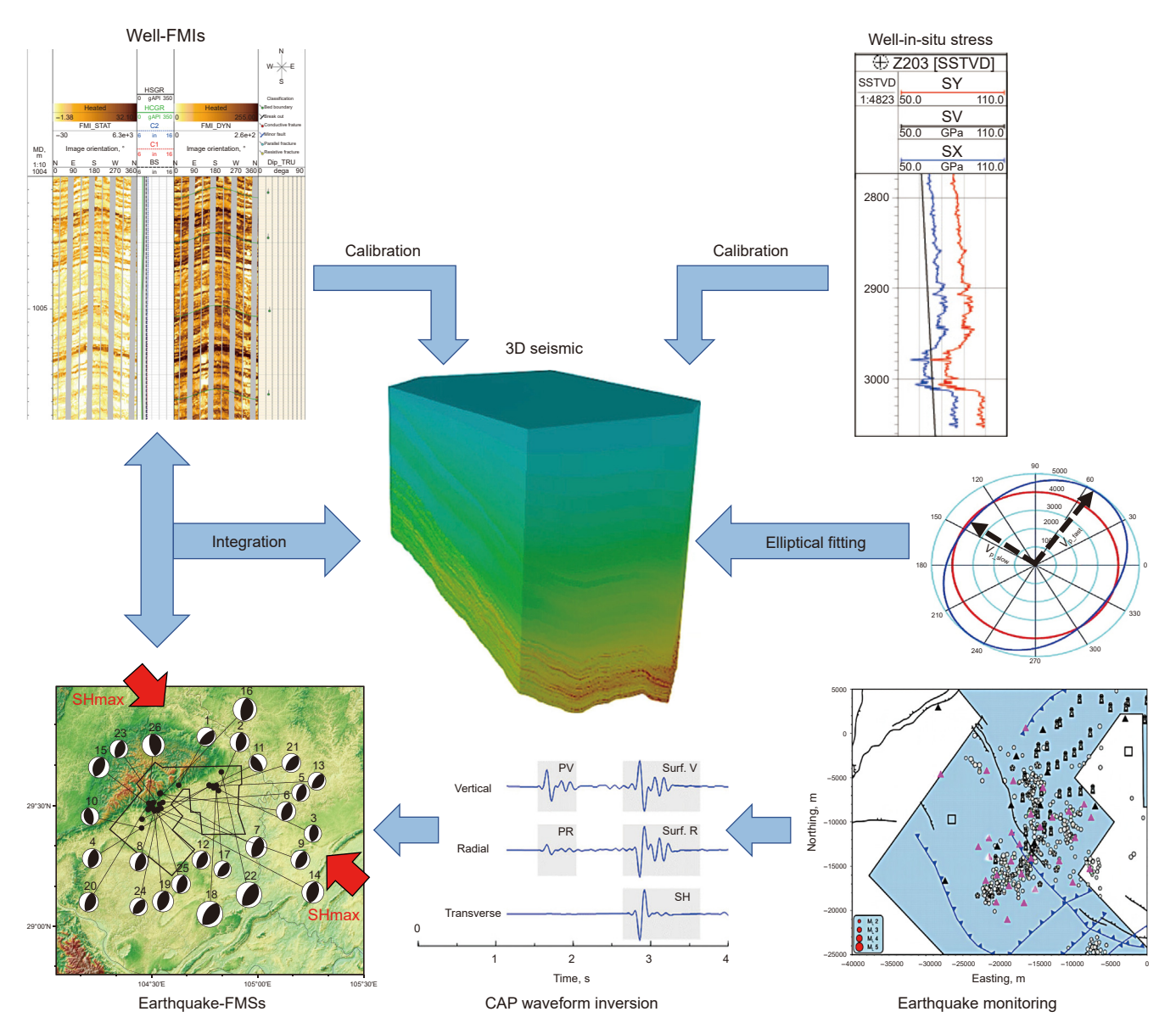


**Fig. 3.** The workflow for integrating data from multiple scales and sources to predict the orientation of the maximum horizontal stress (SHmax). Image logs are characterized as 1D whereas earthquakes introduce 3D complexity. The incorporation of 3D seismic data, which offers comprehensive spatial information, plays a vital role in supplementing and bridging the frequency gaps.

approach. First, the prestack WAZ data is sorted into OVT sectors to perform AVO inversion for each azimuth. Then, the resulting azimuthal P-wave phase velocities are used to calculate anisotropy parameters through elliptical fitting, which includes both the strength and direction of fractures.

The study areas are dominated by vertical/near-vertical faults which can be described as horizontal transversely isotropic (HTI) medium. The P-waves pass through an HTI medium resulting in orientational variations of seismic velocity. The faster P-waves usually propagate parallel to the dominant orientation of azimuthal anisotropy while the slow P-waves are perpendicular. Hence, employing multiple azimuthal shots at consistent offsets facilitates comprehensive coverage, enabling the measurements of azimuthal anisotropy within P-wave velocities (Kimura et al., 2021). Based on the linear slip theory assumes that the direction of the SHmax aligns with a single set of parallel vertical fractures, whereas the SHmin direction is orthogonal to the fractures (Schoenberg and Sayers, 1995). Fig. 7 depicts the correlation between horizontal

stress and alignment fractures. The P-wave phase velocities at different azimuths can be simplified as (Mallick et al., 1998)

$$V_{\rm P}(\phi_i) = A + B\cos[2(\phi_i - \phi_0)], \ i = 1, 2...N,$$
 (1)

where N is the number of azimuth sectors;  $\phi_i$  is the currently observed azimuth of the survey line;  $\phi_0$  is the fast P-wave phase velocity; A is the average of the phase velocity across all azimuth sectors; B is the elliptical coefficient as the function of fracture density. Solving Eq. (1) via the least squares elliptical fitting, we use more than three azimuths to solve A, B and  $\phi_0$ , and obtain the fast and slow P-wave phase velocities.

$$F(A, B, \phi_0) = \sum_{i=1}^{N} [V_P(\phi_i) - A - B \cos[2(\phi_i - \phi_0)]]^2;$$

$$V_{P\_fast} = A + B,$$

$$V_{P\_slow} = A - B.$$
(2)

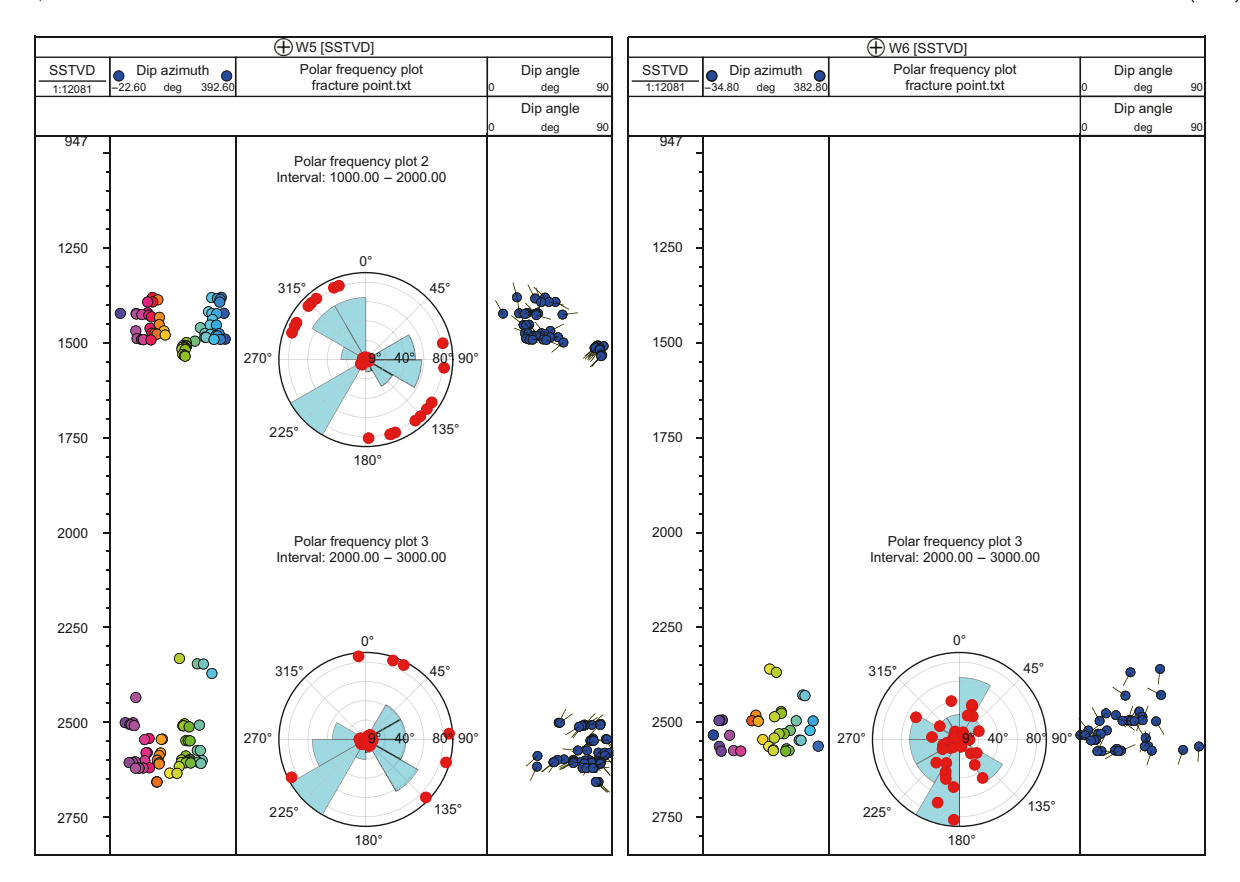


Fig. 4. The orientation and dip of the developed DIFs in two wells. In Well W5, DIFs are observed at approximately 1400 m and 2500 m depth, which indicates a stable direction of SHmax (maximum horizontal stress) with little to no rotation across these depth intervals. On the other hand, in Well W6, DIFs are only detected around the 2500 m depth mark, displaying a distribution pattern that is distinct from the one observed in Well W5. This difference suggests a variation in the stress field influence between the two wells, which could be attributed to local geological structures or changes in rock mechanical properties.

There are three assumptions in calculating the magnitude and direction of stress in this article. Firstly, it is assumed that anisotropy is caused by high-angle fractures, characterized by variations in velocity in different directions. Secondly, it is assumed that the orientation of these fractures aligns with the direction of the maximum horizontal principal stress (SHmax). The SHmax orientation is indirectly inferred from the fracture orientation, which is derived from azimuthal velocity anisotropy. Thirdly, it is assumed that the stress direction has remained consistent between ancient and present.

This study estimates the stress direction using elliptical fitting of azimuthal seismic data. Traditional 3D geomechanics often rely on finite element simulation (Li et al., 2024), but their accuracy is affected by factors such as mesh division, boundary conditions, and

computationally inefficient, especially for large-scale geological problems, requiring significant resources and time, thus limiting their scale and scope. Additionally, they typically analyze single geological processes, making it difficult to account for the complexity and diversity of geological systems. Therefore, this study employs seismic data-driven geomechanical modeling techniques, significantly improving stress calculation efficiency. We based on the mechanical earth model (MEM) for calculating the magnitude of in-situ stress. Shuai et al. (2023) used 3D seismic data to estimate in-situ stress based on the curvature attribute integrated MEM. However, this method is limited to isotropic media; we have extended its applicability from isotropy to HTI media and calculated stress orientations. The following expression presents the curvature attribute integrated HTI MEM:

$$\begin{split} \sigma_{h} &= \frac{\nu(1+\nu)}{1+EZ_{N}-\nu^{2}}(\sigma_{V}-\alpha P_{P}) + \frac{Ez}{1+EZ_{N}-\nu^{2}}K_{X} + \frac{\nu Ez}{1+EZ_{N}-\nu^{2}}K_{y} + \alpha P_{P}, \\ \sigma_{H} &= \frac{\nu(1+EZ_{N}+\nu)}{1+EZ_{N}-\nu^{2}}(\sigma_{V}-\alpha P_{P}) + \frac{\nu Ez}{1+EZ_{N}-\nu^{2}}K_{X} + \frac{Ez(1+EZ_{N})}{1+EZ_{N}-\nu^{2}}K_{y} + \alpha P_{P}, \end{split}$$
(3)

model parameters. Handling complex geological structures requires detailed meshing, which increases computational load and cost, while uncertainties in boundary conditions and parameters affect simulation accuracy. Finite element simulations are

where  $\sigma_h$  and  $\sigma_H$  are the SHmin and SHmax integrated curvature attributes in HTI medium;  $\sigma_V$  is the vertical stress;  $K_X$  and  $K_Y$  are the curvature attributes. z is the thickness of the thin plate.  $\alpha$  is the Biot coefficient,  $P_P$  is the pore pressure. E and  $\nu$  are the static Young's

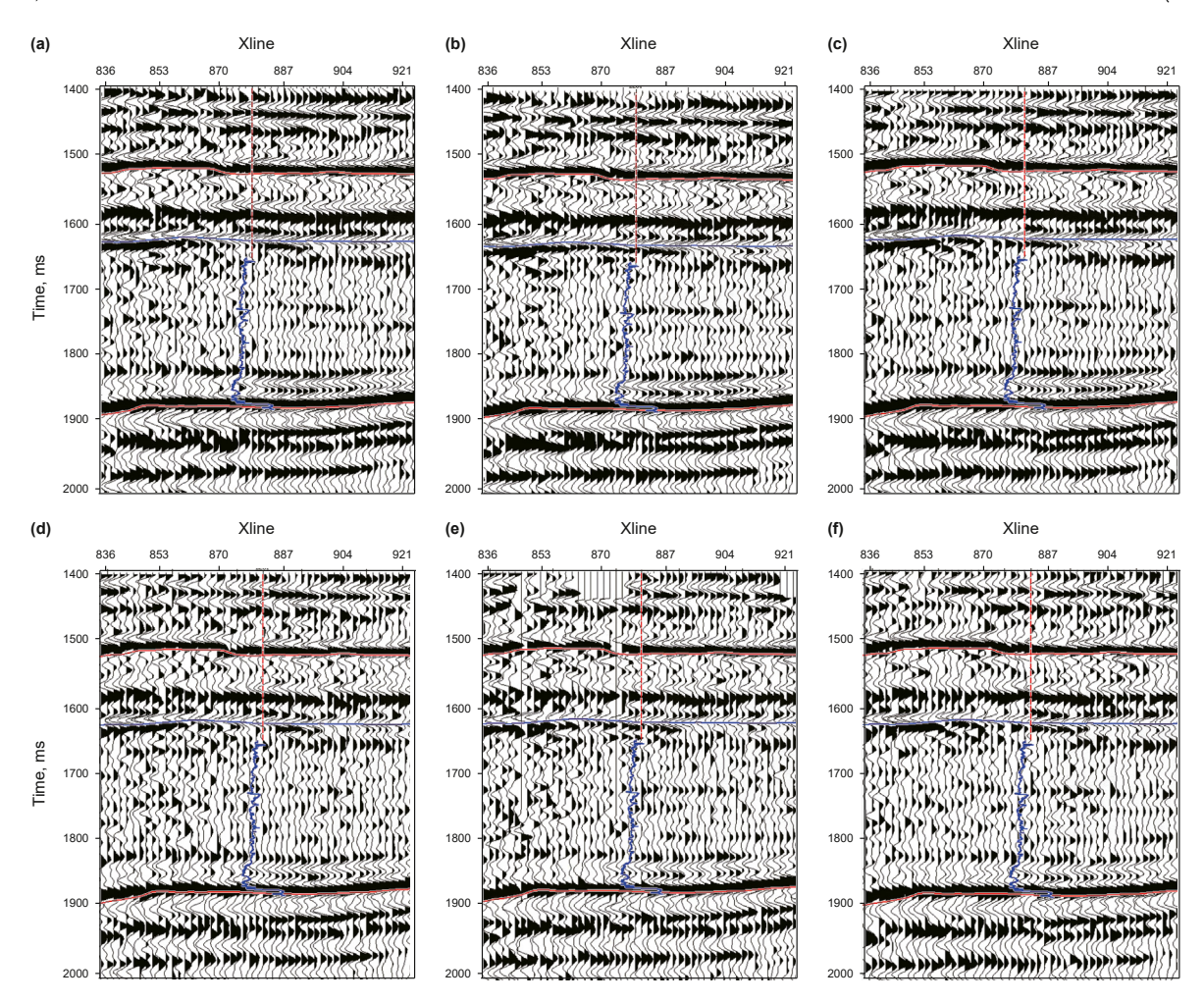


Fig. 5. Display of six different azimuthal sector stacks. The central azimuth angles are (a) 0°, (b) 60°, (c) 120°, (d) 180°, (e) 240°, (f) 300°. This seismic profile across the Well W1, where the blue well is P-wave velocities. It is evident that within the target layer, there exists a low-velocity zone, while the boundary of the target layer is characterized by a high-velocity zone.

modulus, and static Poisson's ratio, respectively.  $Z_N$  is the normal compliance. It can be written in terms of the fracture weakness for gas-filled as (Bakulin et al., 2000)

$$Z_{\rm N} = \frac{4e}{V_{\rm P}^2[3g(1-g)-4e]},\tag{4}$$

where e is fracture density used ellipse fitting.  $g = \frac{V_P^2}{V_P^2}$ ;  $V_P$  and  $V_S$  are the velocity of the P-wave and S-wave, respectively. In this study, E and v were computed using the  $V_P$ ,  $V_S$ , and  $\rho$ ;  $P_P$  is obtained through the Bowers method (Bowers, 1995); the finite difference method is employed to calculate the curvature attributes of  $K_X$  and  $K_Y$  within the seismic volume (Peet and Sahota, 1985; Shuai et al., 2023). Fig. 8 illustrates the original in-situ stress field and direction. The model encompasses an area of 1000 km², featuring a grid size of 30.89 million cells and modeling depth of 0–5 km.

#### 3.3. Earthquake and FMSs

In this study, the FMSs as shown in Table 1 by the Sichuan Seismic Network Center in the Weiyuan area, China, started in 2016. The FMSs in Fig. 9(a) reveal that the predominant earthquake events in this region are characterized by reverse-faulting. This orientation of the P-axis is shown in Fig. 9(c), trends in the NW-SE

direction, which alignment correlates with the orientation of the SHmax (Fig. 9(b)) within the regional tectonic stress field.

#### 4. Results and discussion

The workflow delineates the process for calculating the magnitude and direction of in-situ stress integrating multi-source data such as 3D seismic, earthquakes, and well logs to establish a comprehensive 3D in-situ stress model in the Weiyuan area as shown in Fig. 10.

## 4.1. The orientation of P-axis and SHmax

To describe the fault parameters in terms of the P-axis, B-axis (null axis), and T-axis (tension axis) angles, two coordinate system rotations are necessary. Initially, the principal stress coordinate system is transformed into the geographical coordinate system, both of which are right-handed systems. Subsequently, the fault plane coordinate system is established, consisting of the Sd (dip), Ss (strike), and Sn (normal) vectors. We can obtain the displacement (or slip) vector **d** on the fault plane and its normal vector **n**, as shown in Eqs. (5) and (6):

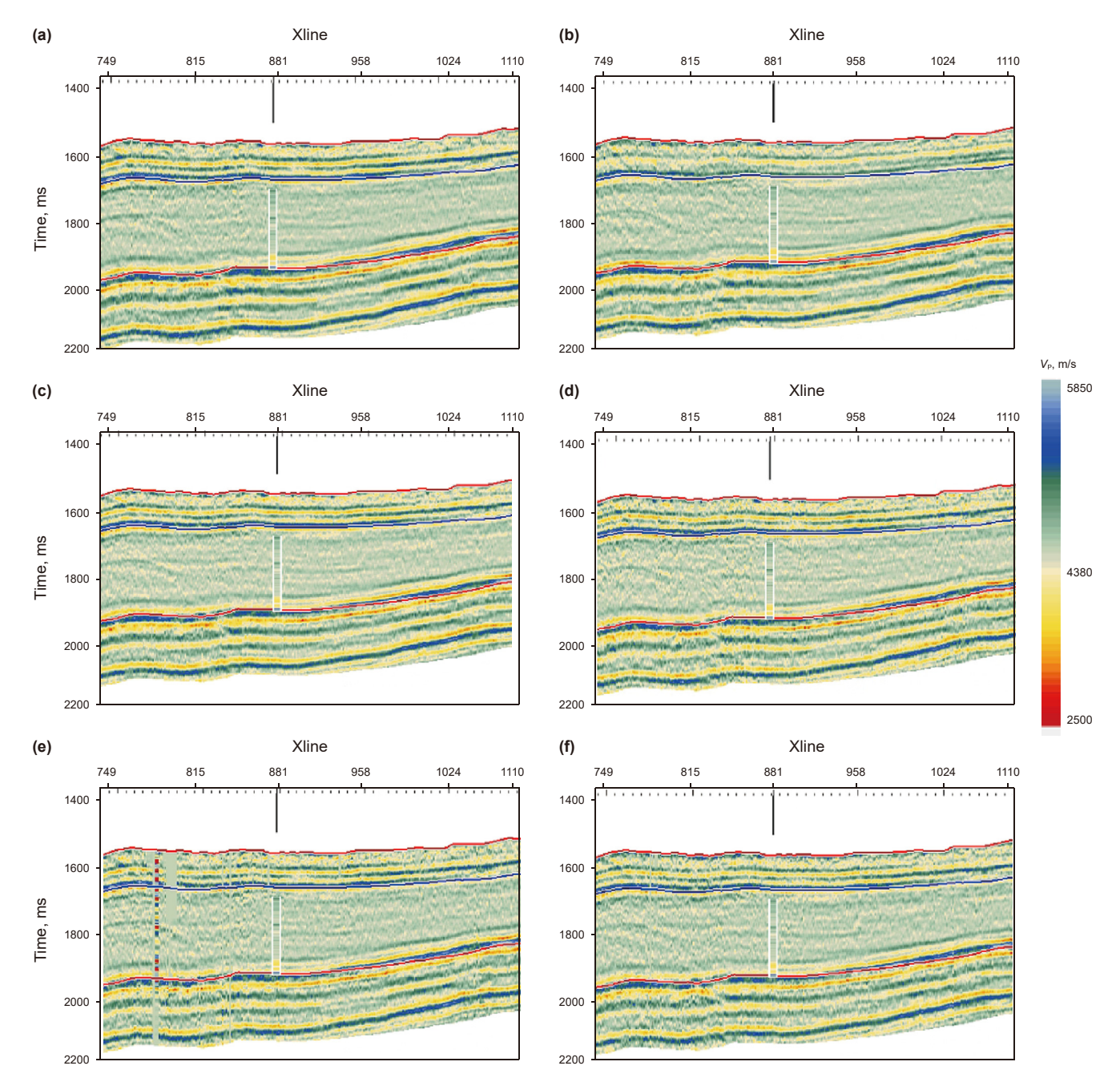


**Fig. 6.** The six azimuth's P-wave phase velocities. The central azimuth angles are **(a)** 0°, **(b)** 60°, **(c)** 120°, **(d)** 180°, **(e)** 240°, **(f)** 300°. The P-wave phase velocities profiles show an excellent agreement with the well.

$$\mathbf{d} = \begin{pmatrix} \cos(\theta_{s})\cos(\lambda_{s}) + \sin(\theta_{s})\cos(\delta_{s})\sin(\lambda_{s}) \\ \sin(\theta_{s})\cos(\lambda_{s}) - \cos(\theta_{s})\cos(\delta_{s})\sin(\lambda_{s}) \\ -\sin(\delta_{s})\sin(\lambda_{s}) \end{pmatrix}, \tag{5}$$

$$\mathbf{n} = \begin{pmatrix} -\sin(\theta_{s})\sin(dip) \\ \cos(\theta_{s})\sin(dip) \\ -\cos(dip) \end{pmatrix}, \tag{6}$$

where  $\theta_s$ ,  $\delta_s$ , and  $\lambda_s$  represent the strike, dip, and rake angle of the fault, respectively. The eigenvectors of the moment tensor align with the principal axes, which can be characterized by the displacement and normal vectors (Hudson et al., 1989):

$$T = \frac{1}{\sqrt{2}}(\mathbf{n} + \mathbf{d}),$$

$$P = \frac{1}{\sqrt{2}}(\mathbf{n} + \mathbf{d}).$$
(7)

Based on the results from Fig. 9, we extracted the SHmax orientation of the 3D seismic of the O<sub>3</sub>w Formation. We compared SHmax orientations with the P-axis of 12 earthquakes. The depths of the earthquakes were approximately 3 km. The comparison revealed a good agreement between the two as shown in Fig. 11.

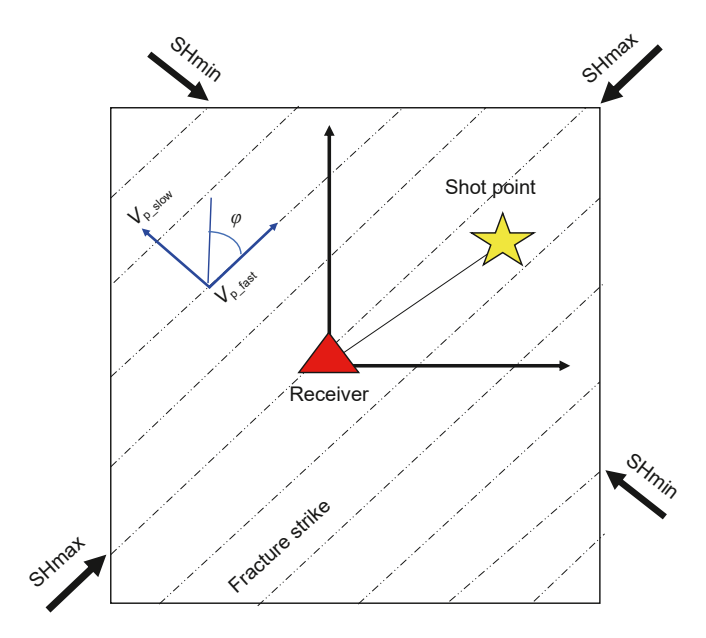


**Fig. 7.** Schematic drawing of the multi-azimuth survey in an anisotropic medium (Kimura et al., 2021). The fast P-wave's polarization azimuth typically aligns with the orientation of SHmax.

#### 4.2. The 3D stress model

We compare the orientation of the P-axis and the direction of SHmax associated with the 12 earthquakes in Fig. 12. Fig. 12(a) depicts a comparative analysis between the directions of SHmax and the P-axis. The majority of these directions exhibit a strong alignment, showcasing a prominent agreement. However, a distinct subset (vellow arrows) reveals instances where a rotation of nearly 90° has occurred. We are considering the broad-scale advantage of the FMSs and utilizing them to constrain the orientation of the SHmax via co-kriging. Fig. 12(b) illustrates a comparison between the directions of SHmax constrained by the FMSs. This comparison serves to effectively discern and quantify the advantages inherent in our method. Table 2 offers comprehensive results for the P-axis, SHmax, and the SHmax direction after correction using FMSs. The first column contains earthquake event numbers, followed by longitude and latitude in the second and third columns, respectively. The fourth column represents the P-axis, while the fifth column denotes SHmax obtained from 3D seismic data. The sixth column indicates SHmax integrated with full-scale information, and the seventh column quantifies the discrepancy between the integrated SHmax and the P-axis. For enhanced clarity and intuitive interpretation, we standardized the directions to a range of 0–180°, as demonstrated in Table 3.

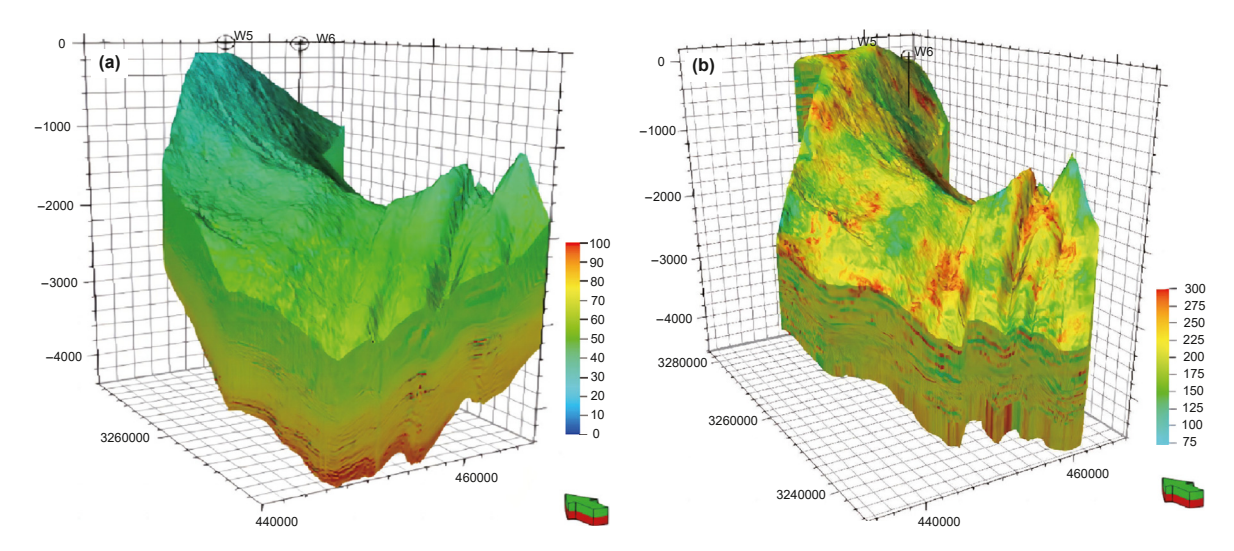


Fig. 8. Original stress model and stress direction model. (a) is the magnitude of in-situ stress; (b) indicates the direction of in-situ stress. Due to variations in the size of the study area, the grid resolution for stress magnitude and direction differs between the two regions: (a) encompasses 30.89 million grids, while (b) comprises 24.40 million grids.

**Table 1** Focal mechanism source solutions (Yi et al., 2020).

Nr	Date	Time	Lat	Lon	depth	M	Strike	Dip	Rake
1	2016-01-07	04:17:59.9	104.6274	29.5836	3	3.7	47	22	90
2	2018-07-22	22:43:49.8	104.5382	29.5486	2	3.8	21	36	91
3	2018-07-22	23:02:03.1	104.5410	29.5521	1.5	4.2	23	32	93
4	2018-10-23	06:44:28.8	104.4525	29.4072	3.5	3.5	350	57	94
5	2019-01-23	06:40:36.8	104.4941	29.4919	3	3.6	26	33	89
6	2019-02-23	21:38:09.6	104.5072	29.4865	2.5	4.3	17	47	91
7	2019-02-25	00:40:26.6	104.5030	29.4926	2.5	4.1	27	49	97
8	2019-02-25	05:15:58.9	104.4860	29.4869	2	4.6	13	29	93
9	2019-09-08	02:36:22.6	104.5080	29.5112	2	4.1	26	46	100
10	2019-09-09	17:27:43.5	104.4865	29.5099	2	3.8	29	30	100
11	2019-12-30	01:24:56.9	104.5370	29.5060	3	3.5	41	37	94
12	2020-02-15	20:28:19.8	104.4833	29.4833	2.5	4.4	1	29	101

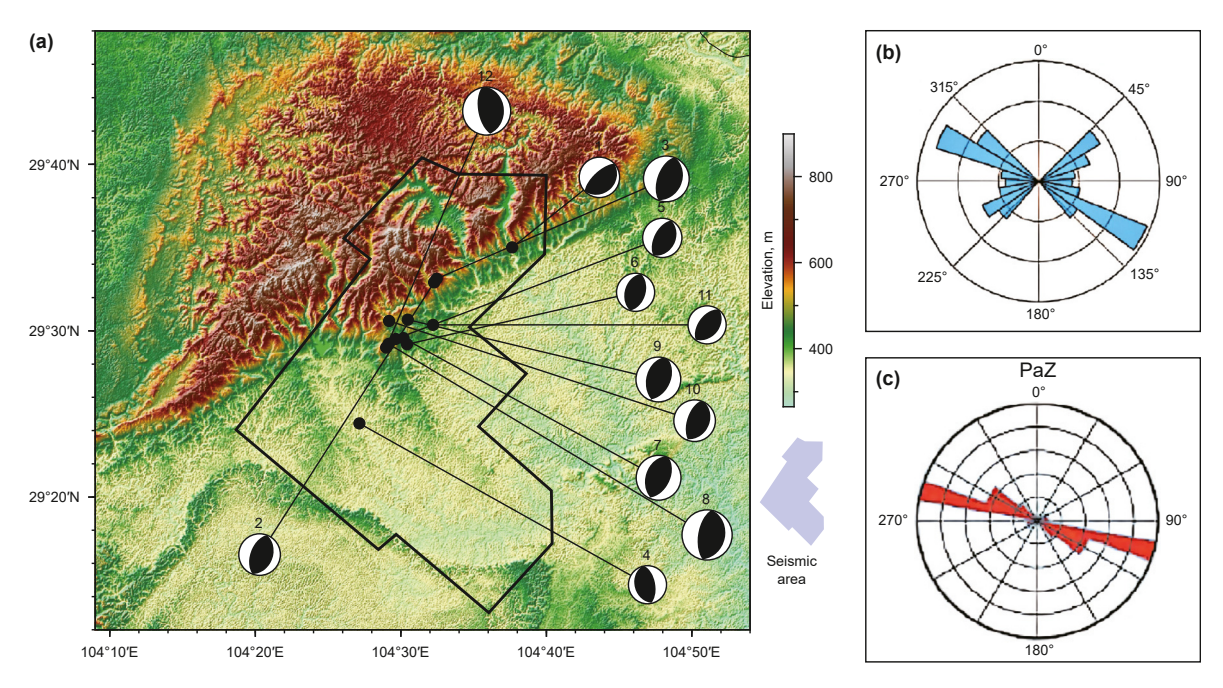
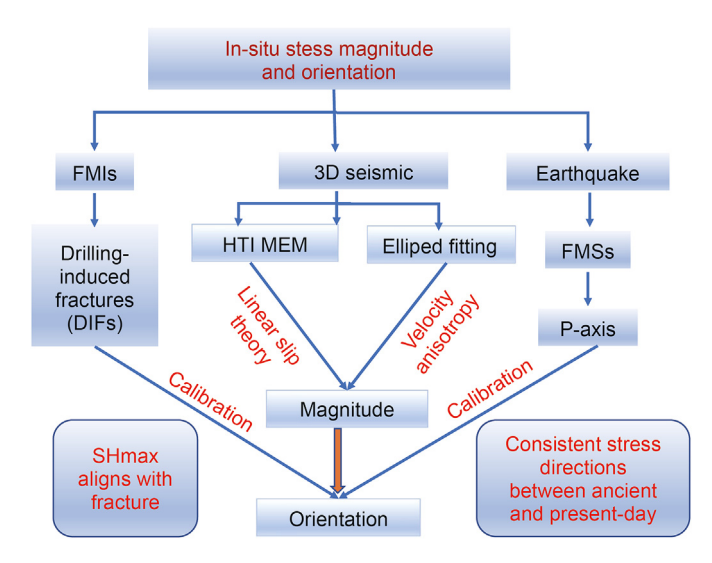


Fig. 9. (a) represents the FMSs, primarily characterized by the reverse faulting predominating in the Weiyuan area. (b) represents the comprehensive orientation of SHmax, while (c) denotes the direction of the P-axis (Yi et al., 2020).



**Fig. 10.** The workflow outlines the magnitude and orientation of in-situ stress by integrating multi-source data. This integration aims to establish a comprehensive 3D in-situ stress model tailored to the geological conditions in the Weiyuan area.

The 3D in-situ stress results, incorporating information from FMSs, FMIs, and seismic velocity anisotropic shown in Fig. 13. These integrated data sources provide a comprehensive understanding of the subsurface stress regime, allowing for accurate determination of the orientation and magnitude of the principal stresses. The FMS and FMI logs contribute detailed fracture and borehole image data, while the seismic velocity anisotropy offers insights into the stress-induced changes in wave propagation characteristics. Together, these datasets enhance the resolution and reliability of the 3D stress model, facilitating improved predictions and analyses of subsurface stress conditions.

The proposed methodology integrates 3D seismic, FMSs, and FMIs to calculate the SHmax direction. These methods exhibit significant disparities in their temporal and spatial distributions.

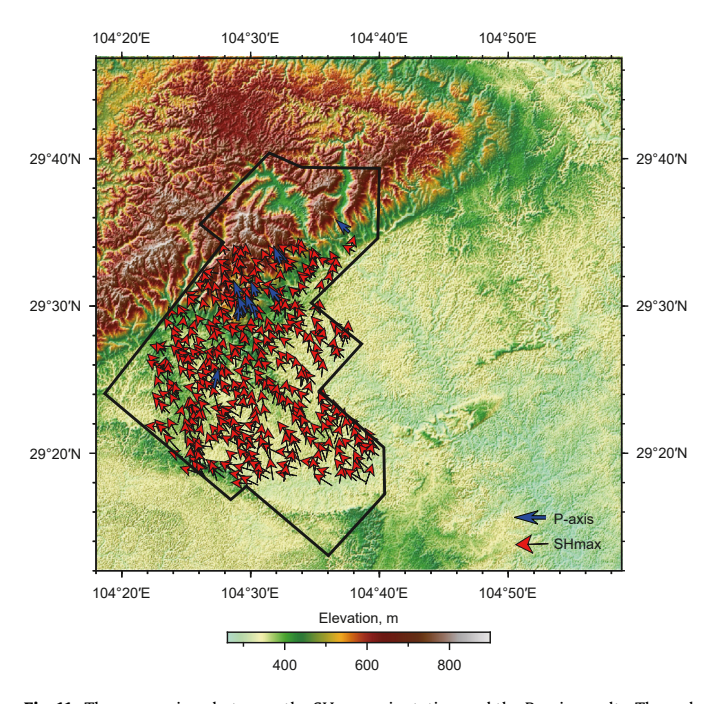


**Fig. 11.** The comparison between the SHmax orientation and the P-axis results. The red triangle signifies the SHmax direction at the  $O_3$ w Formation, and downsampling to 592 grid points. while the blue arrow denotes the P-axis direction. Notably, the primary orientation of SHmax lies in the NW-SE direction, demonstrating a favorable alignment with the P-axis direction. We standardize the P-axis and SHmax directions to a range between 0 and  $180^\circ$ .

We summarize the pros and cons of these methods in Table 4.

FMI technology offers high-definition imaging of minute geological structures and faults, enabling real-time data capture for ongoing analysis during drilling operations. This facilitates drilling decisions informed by local geological contexts. Nonetheless, the technology is not without its constraints, which include the provision of limited information primarily restricted to the vicinity of



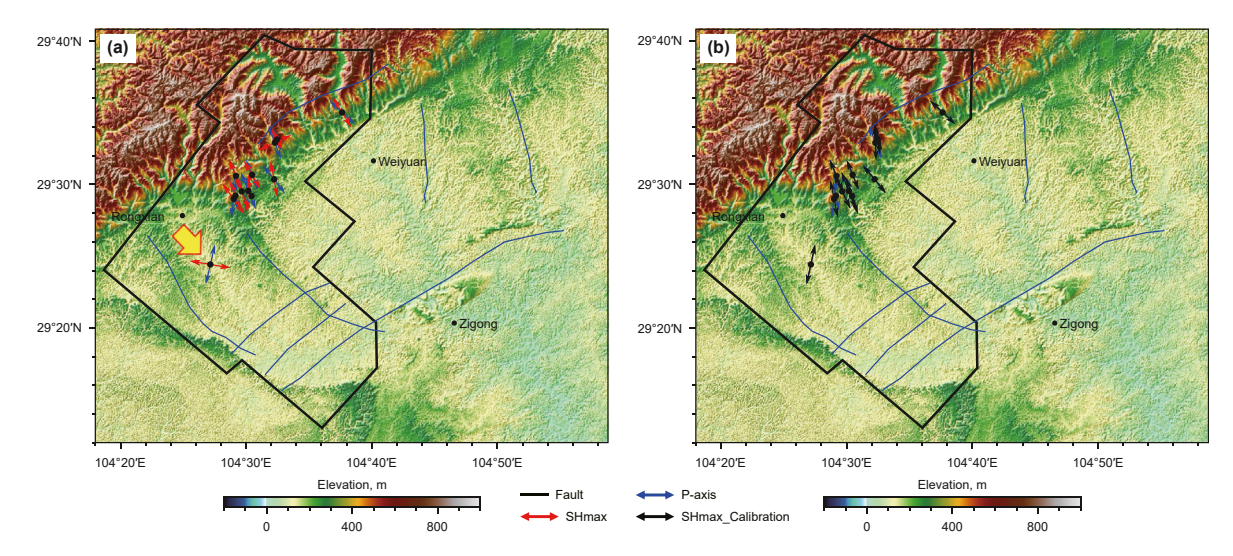


Fig. 12. (a) This presents a comparison between the directions of SHmax and P-axis, revealing a local stress direction rotation of approximately 90°. (b) The result of the SHmax is constrained by FMSs and the P-axis, demonstrating a strong alignment between the two.

**Table 2**Comparison between the orientation of 3D SHmax and the P-axis results.

Nr	Lat	Lon	P-axis, °	SHmax, °	Calibration	Difference
8	104.4860	29.4869	290.82	297.00	291.88	1.06
3	104.5410	29.5521	280.79	290.56	279.70	-1.09
9	104.5080	29.5112	112.05	300.29	112.00	-0.05
4	104.4525	29.4072	77.11	170.31	78.25	1.14
12	104.4833	29.4833	262.92	305.77	281.26	18.34
6	104.5072	29.4865	106.29	105.82	108.01	1.72
5	104.4941	29.4919	296.72	301.70	295.54	-1.18
7	104.5030	29.4926	112.05	264.79	110.99	-1.06
11	104.5370	29.5060	308.14	280.77	310.07	1.93
10	104.4865	29.5099	291.69	292.53	293.17	1.48
2	104.5382	29.5486	290.28	204.57	271.98	-18.30
1	104.6274	29.5836	317.00	301.52	316.78	-0.22

Table 3 The normalized results for the 3D SHmax direction and P-axis direction, range from 0 to  $180^{\circ}$ .

Nr	Lat	Lon	P-axis, °	SHmax, °	Calibration	Difference
8	104.4860	29.4869	110.82	117.00	111.88	1.06
3	104.5410	29.5521	100.79	110.56	99.70	-1.09
9	104.5080	29.5112	112.05	120.29	112.00	-0.05
4	104.4525	29.4072	77.11	170.31	78.25	1.14
12	104.4833	29.4833	82.92	305.77	101.26	18.34
6	104.5072	29.4865	106.29	105.82	108.01	1.72
5	104.4941	29.4919	116.72	121.70	115.54	-1.18
7	104.5030	29.4926	112.05	84.79	110.99	-1.06
11	104.5370	29.5060	128.14	100.77	130.07	1.93
10	104.4865	29.5099	111.69	112.53	113.17	1.48
2	104.5382	29.5486	110.28	24.57	91.98	-18.30
1	104.6274	29.5836	137.00	121.52	136.78	-0.22

the wellbore. Additionally, the quality of the imaging is susceptible to the influences of wellbore conditions and rock characteristics, coupled with the considerable costs associated with its application. The efficacy of focal mechanism solutions is found in their capacity to expose fault structures, rupture patterns, and the orientation of stress. Nevertheless, they are hampered by imprecision in determining the depth of earthquakes and limited capability in defining the focal mechanisms for earthquakes of lower magnitude.

The orientation of the P-axis and SHmax exhibits several discrepancies, as highlighted by the yellow arrow in Fig. 12 prompting

us to speculate that the observed characteristics at this location could be influenced by the presence of a fault. Fault activity may cause alterations in the local stress field, leading to regional bending and deformation, which could consequently result in a change in the orientation of SHmax. Additionally, there might be a stress transfer effect associated with the fault, contributing to a reorientation of the principal stress axis in the fault's vicinity. We propose several potential explanations for this behavior: (1) Intricate tectonic settings, including ongoing faulting activities, structural complexities, or non-uniform stress fields; (2) non-uniform geological settings, such as tilted strata or diverse geological structures; (3) specific geological conditions, like localized rock layers or heterogeneity, could create a localized stress field demonstrating deviation from the stress field governed by the principal P-axis.

Our approach is founded on two key assumptions: firstly, it employs a linear slip theory, positing that the fracture direction coincides with the SHmax direction; secondly, it assumes a consistency in stress direction between past and present-day conditions.

#### 5. Conclusions

In this paper, we incorporate 3D seismic data with active sources as a lateral constraint to approximate the 3D orientation field of insitu stress. Specifically, considering the strong correlation between stress and fractures with velocity anisotropy, we derive the azimuthal anisotropy orientation from multi-azimuth 3D seismic data to compensate for the spatial gaps in stress orientations. Utilizing field examples from the Weiyuan area in the Sichuan Basin, China, a shale-gas production region, we demonstrate our workflow. Integration of multi-source data, including 3D seismic, passive monitoring, and well logs, is employed to establish a comprehensive 3D in-situ stress model. The 3D seismic results validate our assumption that the estimated anisotropy orientations closely match the direction of the SHmax obtained from FMIs. We analyzed 26 earthquakes (ML > 3) recorded from 2016 to 2020 to calculate the FMSs. The resulting SHmax direction in the 3D stress model is determined as 110° ES, closely aligning with FMSs (<3.96°). This alignment underscores the reliability and accuracy of our integration method in predicting the 3D SHmax orientation. We have drawn the following conclusions in the Sichuan Basin of the



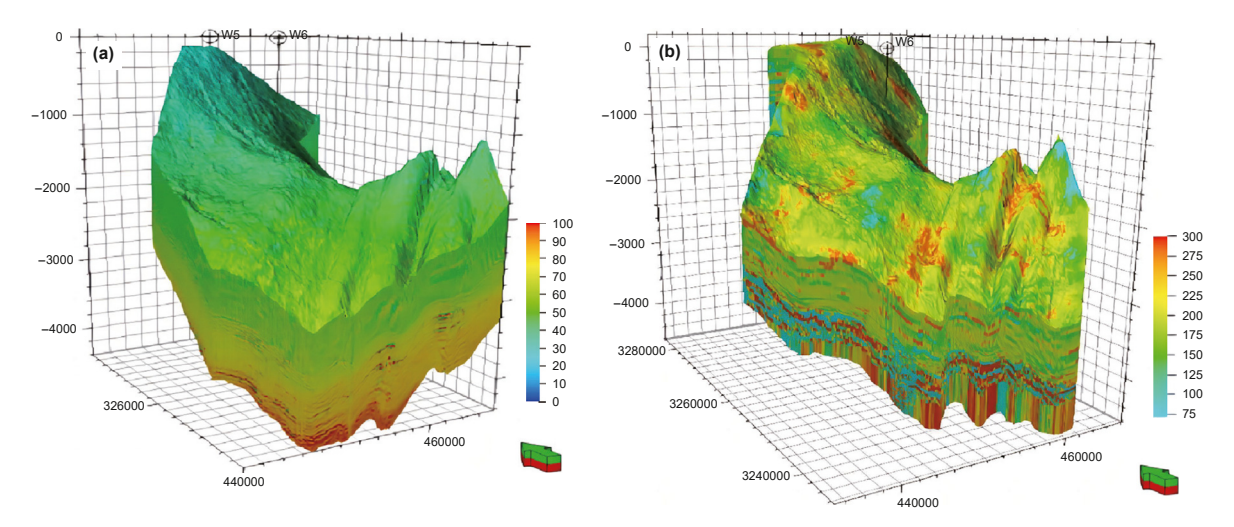


Fig. 13. The in-situ stress model integrated FMSs, FMIs, and 3D seismic. (a) and (b) respectively represent the 3D magnitude and direction of the in-situ stress. The stress magnitude remains consistent with the original stress, while the deviation in stress direction from the original is attributed to the inclusion of constraints derived from FMSs.

**Table 4**The comparison between FMIs, FMSs, and 3D seismic.

Method	Scale	Assumption	Advantages	Disadvantages	Cost
FMIs	Small	Drilling-induced fracture	High-resolution, real- time acquisition	Localized information, influenced by wellbore conditions	High
FMSs	Large	Circular symmetric rupture source, uniform isotropic medium, neglect of propagation path effects	Large-scale, fault structure	Inaccurate seismogenic depth	Low
3D seismic	Middle	e Pure elastic, continuous medium, static equilibrium,	3D spatial continuity	Indirect assessment for stress direction	Middle

#### Weiyuan area.

- (1) We infer that the Weiyuan area is within a relatively complex tectonic stress setting. The P-axis derived from the inversion of the regional stress field shows a direction trending NW-SE, nearly horizontal, this alignment aligns closely with the SHmax direction of the tectonic stress field in the region, illustrating that tectonic activity in the area is predominantly governed by the regional tectonic stress field.
- (2) High-precision logging imaging of FMI data and the comprehensive FMSs across the region exhibit certain discrepancies, signaling the intricate and complex nature of the stress and tectonic environment in the area.
- (3) The combined application of seismic velocity anisotropy, FMIs, and FMSs provides multifaceted constraints on the current principal stress orientation, offering a profound understanding of the fault environment in the region. This method ingeniously integrates seismic data, well-logging information, and FMSs multidimensional datasets, forming a comprehensive framework of full-scale information. It contributes to a more comprehensive and in-depth insight into the geological structure and stress environment, enhancing the study of the regional geological and tectonic conditions.

In future work, we plan to focus on improving the model parameters and resolution, to validate the model's applicability and reliability under different geological conditions. At the same time, we will develop a 4D dynamic stress field model that accounts for changes in stress conditions over time. By integrating stress drop parameters from FMSs, we aim to predict 4D stress field changes due to fault disturbances.

#### Conflict of interest

No potential conflict of interest was reported by the authors.

## CRediT authorship contribution statement

**Huan Cao:** Writing — original draft, Methodology. **Yang Zhao:** Writing — review & editing, Methodology. **Hai-Chao Chen:** Writing — review & editing. **Le-Le Zhang:** Writing — review & editing. **Cheng-Gang Xian:** Writing — review & editing. **Ji-Dong Yang:** Writing — review & editing. **Lu Liu:** Writing — review & editing.

### Acknowledgment

We would like to thank PetroChina Xinan Company for providing us with the seismic data and permitting us to publish the results. We appreciate the editor and the anonymous reviewers for their constructive comments and suggestions, which significantly improved the quality of this paper. This study is jointly supported by the National Key R&D Program of China (Grant No. 2020YFA0710604) and NSFC (Grant No. 42374064).

#### References

Amemoutou, A., Martínez-Garzón, P., Kwiatek, G., Rubinstein, J.L., Bohnhoff, M., 2021. Earthquake source mechanisms and stress field variations associated with wastewater-induced seismicity in Southern Kansas, USA. J. Geophys. Res. Solid Earth 126 (7), e2020JB021625. https://doi.org/10.1029/2020JB021625.

Bakulin, A., Grechka, V., Tsvankin, I., 2000. Estimation of fracture parameters from reflection seismic data—Part I: HTI model due to a single fracture set. Geophysics 65 (6), 1788–1802. https://doi.org/10.1190/1.1444863.

Bao, H., Sun, L., Yu, L., Zhang, H., 2009. Obtainment of ground stress by Kaiser effect of rock acoustic emission. Duankuai Youqitian 16 (6), 94–96 (in Chinese). doi: 1005-8907(2009)06-094-03.

Bowers, G.L., 1995. Pore pressure estimation from velocity data: accounting for

- overpressure mechanisms besides undercompaction. SPE Drill & Compl 10 (2), 89–95, https://doi.org/10.2118/27488-PA.
- Chen, H., Innanen, K.A., 2023. Estimating two groups of fracture weaknesses using azimuthal differences in partially incidence-angle-stacked seismic amplitudes. Geophysics 88 (4), 1–67. https://doi.org/10.1190/geo2022-0541.1.
- Chu, R., Sheng, M., 2023. Stress features inferred from induced earthquakes in the Weiyuan shale gas block in Southwestern China. J. Geophys. Res. Solid Earth 128 (2), e2022|B025344. https://doi.org/10.1029/2022|B025344.
- Cornet, F.H., Valette, B., 1984. In situ stress determination from hydraulic injection test data. J. Geophys. Res. Solid Earth 89 (B13), 11527–11537. https://doi.org/10.1029/IB089iB13p11527.
- Cui, J., Lin, W., Wang, L., Gao, L., Huang, Y., Wang, W., et al., 2014. Determination of three-dimensional in situ stresses by anelastic strain recovery in wenchuan earthquake fault Scientific drilling project hole-1 (WFSD-1). Tectonophysics 619–620, 123–132. https://doi.org/10.1016/j.tecto.2013.09.013.
- Delorey, A.A., Bokelmann, G.H.R., Johnson, C.W., Johnson, P.A., 2021. Estimation of the orientation of stress in the Earth's crust without earthquake or borehole data. Communications Earth & Environment 2 (1), 190. https://doi.org/10.1038/ s43747-021-00244-1
- Ezati, M., Soleimani, B., 2014. Fracture and horizontal stress analysis of Dalan Formation using FMI image log in one of southwestern Iranian oil wells. J. Tethys 2 (1), 1–8.
- Feng, Y., Li, X., Gray, K.E., 2018. Modeling field injectivity tests and implications for in situ stress determination. Int. J. GeoMech. 18 (9), 04018101. https://doi.org/ 10.1061/(ASCE)GM.1943-5622.0001231.
- Haimson, B., Fairhurst, C., 1967. Initiation and extension of hydraulic fractures in rocks. Soc. Petrol. Eng. J. 7 (3), 310–318. https://doi.org/10.2118/1710-PA.
- Haimson, B.C., Song, I., 1995. A new borehole failure criterion for estimating in situ stress from breakout span. In: 8th ISRM Congress Tokyo, Japan pp. ISRM-8CONGRESS-1995-071.
- Han, Y., Feng, Y., Li, X., Zhang, S., 2020. Evaluation of in-situ stress orientation: a laboratory approach combining paleomagnetic test and acoustic anisotropy test. J. Petrol. Sci. Eng. 195, 107870. https://doi.org/10.1016/j.petrol.2020.107870.
- Heidbach, O., Rajabi, M., Cui, X., et al., 2018. The World Stress Map database release 2016: crustal stress pattern across scales. Tectonophysics 744, 484–498. https://doi.org/10.1016/j.tecto.2018.07.007.
- Hornby, B.E., 1989. Imaging of near-borehole structure using full-waveform sonic data. Geophysics 54 (6), 747–757. https://doi.org/10.1190/1.1442702.
- Hou, B., Cheng, W., Chen, M., Tan, P., Yang, L., 2014. Experiments on the non-planar extension of hydraulic fractures in fractured shale gas reservoirs. Nat. Gas. Ind. 34 (12), 81–86.
- Hudson, J.A., Pearce, R.G., Rogers, R.M., 1989. Source type plot for inversion of the moment tensor. J. Geophys. Res. Solid Earth 94 (B1), 765–774. https://doi.org/ 10.1029/JB094iB01p00765.
- Jonaghani, H.H., Manshad, A.K., Ali, J.A., et al., 2019. Fracture analysis and in situ stress estimation of a gas condensate field in Persian Gulf using FMI and DSI image logs. SN Appl. Sci. 1 (11), 1481. https://doi.org/10.1007/s42452-019-1466-4
- Kaiser, A.D., 1957. Mutations in a temperate bacteriophage affecting its ability to lysogenize Escherichia coli. Virology 3 (1), 42–61. https://doi.org/10.1016/0042-6822(57)90022-3.
- Kimura, T., Mikada, H., Araki, E., Kodaira, S., Miura, S., Takahashi, N., 2021. Stress field estimation from s-wave anisotropy observed in multi-azimuth seismic survey with cabled seafloor seismometers above the Nankai Trough Megathrust Zone, Japan. J. Geophys. Res. Solid Earth 126 (9). https://doi.org/10.1029/ 2020IB021380
- Laubach, S.E., Clift, S.J., Hill, R.E., Fix, J., 1992. Stress directions in cretaceous frontier formation, Green River Basin, Wyoming. Wyoming Geological Association. Retrieved from. http://archives.datapages.com/data/wga/data/052/052001/75\_ wga0520075.htm.
- Leeman, E.R., 1964. The measurement of stress in rock: Part II: borehole rock stress measuring instruments. Journal of the Southern African Institute of Mining and Metallurgy 65 (2), 82–114. https://doi.org/10.10520/AJA0038223X\_4883.
- Li, G.Q., Wang, Y., Chen, J.H., et al., 2012. Analysis of the maximum horizontal principal stress based on wellbore collapse information. Petrol. Drill. Tech. 40 (1), 37–41. https://doi.org/10.3969/j.issn.1001-0890.2012.01.008 (in Chinese).
- Li, P., Cai, M., Miao, S., Li, Y., Sun, L., Wang, J., Gorjian, M., 2024. Accurate measurement techniques and prediction approaches for the in-situ rock stress. Sci.

- Rep. 14 (1), 13226. https://doi.org/10.1038/s41598-024-64030-7.
- Liu, N., Wang, G., 2016. Shale gas sweet spot identification and precise geo-steering drilling in Weiyuan Block of Sichuan Basin, SW China. Petrol. Explor. Dev. 43 (6), 1067–1075. https://doi.org/10.1016/S1876-3804(16)30124-0.
- Long, F., Yi, G., Wang, S., Qi, Y., Zhao, M., 2019. Geometry and tectonic deformation of the seismogenic structure for the 8 August 2017 MS 7.0 Jiuzhaigou earthquake sequence, northern Sichuan, China. Earth and Planetary Physics 3 (3), 253–267. https://doi.org/10.26464/epp2019027.
- Lundstern, J.-E., Zoback, M.D., 2016. State of stress in Texas: implications for induced seismicity. Geophys. Res. Lett. 43 (19), 10208–10214. https://doi.org/10.1002/ 2016GL070974.
- Lundstern, J.-E., Zoback, M.D., 2020. Multiscale variations of the crustal stress field throughout North America. Nat. Commun. 11 (1), 1951. https://doi.org/10.1038/ s41467-020-15841-5.
- Mallick, S., Craft, K.L., Meister, L.J., Chambers, R.E., 1998. Determination of the principal directions of azimuthal anisotropy from P-wave seismic data. Geophysics 63 (2), 692–706. https://doi.org/10.1190/1.1444369.
- Pan, X., Li, L., Zhou, S., Zhang, G., Liu, J., 2021. Azimuthal amplitude variation with offset parameterization and inversion for fracture weaknesses in tilted transversely isotropic media. Geophysics 86 (1), C1–C18. https://doi.org/10.1190/geo2019-02151
- Paul, S., Ali, M., Chatterjee, R., 2018. Prediction of compressional wave velocity using regression and neural network modeling and estimation of stress orientation in Bokaro Coalfield, India. Pure Appl. Geophys. 175 (1), 375–388. https://doi.org/ 10.1007/s00024-017-1672-1.
- Peet, F.G., Sahota, T.S., 1985. Surface curvature as a measure of image texture. IEEE Trans. Pattern Anal. Mach. Intell. PAMI-7 (6), 734–738. https://doi.org/10.1109/TPAMI.1985.4767733.
- Schoenberg, M., Sayers, C.M., 1995. Seismic anisotropy of fractured rock. Geophysics 60 (1), 204–211. https://doi.org/10.1190/1.1443748.
- Sheng, M., Chu, R., Peng, Z., Wei, Z., Zeng, X., Wang, Q., Wang, Y., 2022. Earthquakes triggered by fluid diffusion and boosted by fault reactivation in Weiyuan, China due to hydraulic fracturing. J. Geophys. Res. Solid Earth 127 (5), e2021JB022963. https://doi.org/10.1029/2021JB022963.
- Shuai, D., Xian, C., Zhao, Y., Chen, G., Ge, H., Cao, H., 2023. Using 3-D seismic data to estimate stress based on the curvature attribute integrated mechanical earth model. Geophys. J. Int. 233 (2), 885–899. https://doi.org/10.1093/gji/ggac489.
- Teufel, L.W., 1983. Determination of in-situ stress from anelastic strain recovery measurements of oriented core. In: SPE/DOE Low Permeability Gas Reservoirs Symposium, Denver, Colorado, pp. 421–430. https://doi.org/10.2118/11649-MS.
- Tingay, M.R.P., Hillis, R.R., Morley, C.K., King, R.C., Swarbrick, R.E., Damit, A.R., 2009. Present-day stress and neotectonics of Brunei: implications for petroleum exploration and production. AAPG (Am. Assoc. Pet. Geol.) Bull. 93 (1), 75–100. https://doi.org/10.1306/08080808031.
- Yi, G., Long, F., Liang, J., Zhao, M., Wang, S., 2020. Geometry and tectonic deformation of seismogenic structures in the Rongxian-Weiyuan-Zizhong region, Sichuan Basin: insights from focal mechanism solutions. Chin. J. Geophys. 63 (9), 3275–3291. https://doi.org/10.6038/cjg202000095 (in Chinese).
- Zhang, C., Lin, W., He, M., Tao, Z., Meng, W., 2022. Determining in-situ stress state by anelastic strain recovery method beneath Xiamen: implications for the coastal region of Southeastern China. Rock Mech. Rock Eng. 55 (9), 5687–5703. https:// doi.org/10.1007/s00603-022-02915-7.
- Zhang, C., Li, B., Li, H., He, M., Gan, H., Wang, G., Fan, Y., 2023. Stress estimation in a 3 km-deep geothermal borehole: a snapshot of stress state in Southern Cathaysia block, China. Tectonophysics 864, 230031. https://doi.org/10.1016/j.tecto.2023.230031.
- Zhang, Z., Liang, C., Long, F., Zhao, M., Wang, D., 2022. Spatiotemporal variations of focal mechanism solutions and stress field of the 2019 Changning Ms 6.0 Earthquake Sequence. Front. Earth Sci. 9, 797907. https://doi.org/10.3389/ feart.2021.797907.
- Ziaie, M., Fazaelizadeh, M., Ayatizadeh Tanha, A., Sharifzadegan, A., 2023. Estimation of the horizontal in-situ stress magnitude and azimuth using previous drilling data. Petroleum 9 (3), 352–363. https://doi.org/10.1016/j.petlm.2023.02.006.
- Zoback, M.D., 2007. Reservoir Geomechanics. Cambridge University Press, New York, USA. https://doi.org/10.1017/CBO9780511586477.
- Zou, C., Dong, D., Wang, Y., Li, X., Huang, J., Wang, S., et al., 2015. Shale gas in China: characteristics, challenges and prospects (I). Petrol. Explor. Dev. 42 (6), 753–767. https://doi.org/10.1016/S1876-3804(15)30072-0.